Chemical Scissor-Enabled Synthesis of $Ti_3C_2T_x$ MXene Nanowires for Selective Oxygen Reduction to Hydrogen Peroxide

Jin Zhang,[a] Xinyao Zhang,[a] Weihao Sun,[b] Wuzong Zhou,[b] and Wenbo Yue*[a]

[a] Beijing Key Laboratory of Energy Conversion and Storage Materials, College of Chemistry, Beijing Normal University, Beijing 100875, P. R. China

[b] School of Chemistry, University of St Andrews, St Andrews, Fife KY16 9ST, United Kingdom

*Corresponding author

Email address: wbyue@bnu.edu.cn (W.B. Yue)

Abstract

Transition metal carbides, especially $Ti_3C_2T_x$, display appealing prospects in the field of energy conversion and storage due to the unique combination of good conductivity and abundant functional groups. The physical structure as well as surface terminations of $Ti_3C_2T_x$ have significant impact on its properties when scaling down from 3D bulk to 2D sheets. However, moving toward 1D nanowire remains a great challenge because of the absence of anisotropic skeleton in $Ti_3C_2T_x$. Herein, we demonstrate a facile strategy to convert $Ti_3C_2T_x$ nanosheets into crosslinked $Ti_3C_2T_x$ nanowires in hybrid alkaline solutions. The experimental results and theoretical calculation reveal that both OH^- and O_2 play important roles in the controllable cutting of $Ti_3C_2T_x$ nanosheets into nanowires. Compared to $Ti_3C_2T_x$ nanosheets, crosslinked $Ti_3C_2T_x$ nanowires expose much higher density of active sites at edges and surfaces, making them ideal catalysts

for oxygen reduction reaction (ORR). Unexpectedly, $Ti_3C_2T_x$ nanowires can selectively reduce oxygen through a $2e^-$ pathway to hydrogen peroxide. The structural modulation of MXene opens a new avenue toward improved performance in emerging application fields.

Keywords: Controllable cutting; $Ti_3C_2T_x$ nanowires; etching mechanism; oxygen reduction reaction; hydrogen peroxide production

1. Introduction

MXene is a class of 2D inorganic compounds, which are composed of transition metal carbides, nitrides, or carbonitrides with several atomic layer thicknesses [1,2]. MXene is usually obtained by selectively etching A layer from $M_{n+1}AX_n$, where M is an early transition metal, A is an element of group IIIa or IVa (mainly Al or Si), X is C and/or N, and n=1, 2 or 3 [3,4]. As a typical MXene, accordion-like Ti_3C_2 can be obtained by etching Ti_3AlC_2 with HF or LiF/HCl, and further exfoliated to $Ti_3C_2T_x$ nanosheets through intercalation and ultrasonication, where T stands for termination groups (-H, -F, -O or -OH) and x indicates uncertain amount of surface groups [5,6]. Ti_3C_2 is a star material in energy conversion and storage devices such as Li-ion batteries or other metal-ion (e.g., Na, K) batteries, Li-S batteries and supercapacitors on account of its unique layered structure, high electrical conductivity, high specific surface area and tunable surface functionalities [7-11]. However, the presence of a pronounced inclination towards inter-sheet aggregation of MXene nanosheets through van der Waals forces results in the decrease of catalytic and energy storage performance [12]. Moreover, the catalytic activity of the active sites on the MXene

surface is relatively lower than that at the edges [13]. Therefore, a fast and effective method is required to adjust the structure of MXene to meet the special needs such as the ORR catalytic performance.

Etching 2D nanosheets into 1D nanowires through a chemical tailoring method is one of the effective ways to solve the stacking problem of 2D nanosheets and expose more active sites. Recently, some scientists successfully synthesized a 3D porous framework of $Ti_3C_2T_x$ nanoribbons or their derivatives by etching accordion-like Ti_3C_2 in KOH solution [14-17]. Benefited from the interconnected pore structure and large exposed surface area, $Ti_3C_2T_x$ nanoribbons exhibited superior performance as the anodes for Na/K-ion batteries or the sulfur host for Li-S batteries [18,19]. Besides, $Ti_3C_2T_x$ nanoribbons delivered high hydrogen evolution reaction (HER) activity with a low overpotential of 169 mV [20]. Although $Ti_3C_2T_x$ nanoribbons and its derivatives can be obtained through alkali etching, the etching mechanism and influencing factors have not been revealed, causing inability to the precise control of the $Ti_3C_2T_x$ structure. In addition, the structure-activity relationship between the exposed edge sites and the improved performance of $Ti_3C_2T_x$ nanoribbon has not been well known.

Revealing the formation mechanism of $Ti_3C_2T_x$ nanoribbons is favorable for a better understanding of its composition, structure and intrinsic properties, which can guide the synthesis design as to expand its application areas. Herein, we explore the etching process of $Ti_3C_2T_x$ nanosheets in various alkaline solutions such as KOH, NaOH, $NH_3 \cdot H_2O$ or even in H_2O_2 solution. Moreover, different experimental conditions including the type and concentration of alkaline solutions, reaction times, the presence of O_2 and the thickness of $Ti_3C_2T_x$ nanosheets have been explored, combined with

density functional theory (DFT) calculations, to reveal the etching mechanism of $Ti_3C_2T_x$ nanosheets. It is found that the surface group of $Ti_3C_2T_x$ replaced by -OH in the alkaline solution is an important process to accelerate the fracture of C-Ti bonds. In addition, the concentration of OH^- ions and the presence of O_2 are two key influencing factors for the fracture of C-Ti bonds and the formation of TiO_2. Therefore, by controlling the concentration of alkaline solution and oxygen content, it is possible to synthesize porous $Ti_3C_2T_x$ nanosheets, crosslinked $Ti_3C_2T_x$ nanowires, even $Ti_3C_2T_x$ quantum dots or TiO_2 nanoparticles. The ORR performance of crosslinked $Ti_3C_2T_x$ nanowires is also studied to investigate the structure-activity relationship of $Ti_3C_2T_x$ nanowires. The open 3D porous structure and increased edge sites of $Ti_3C_2T_x$ nanowires facilitate the transport and conversion of oxygen. Therefore, the ORR performance of $Ti_3C_2T_x$ is highly improved after transforming the structure from nanosheet to nanowire. More importantly, the increased edge sites of $Ti_3C_2T_x$ nanowires are conducive to selectively reducing oxygen to hydrogen peroxide through the two-electron ORR pathway, making it a potential catalyst for hydrogen peroxide production. With the in-depth study of the intrinsic properties of $Ti_3C_2T_x$ porous nanosheets and crosslinked nanowires, the application fields of $Ti_3C_2T_x$ would be expanded.

2. Experimental Section

2.1 Sample Preparation

Preparation of $Ti_3C_2T_x$ nanosheets: multi-layered $Ti_3C_2T_x$ powder was synthesized according to the literatures [21,22] and then exfoliated to $Ti_3C_2T_x$ nanosheets (see Supporting Information for details).

Etching $Ti_3C_2T_x$ in strong alkaline solution: crosslinked $Ti_3C_2T_x$ nanowires are usually synthesized by etching thin $Ti_3C_2T_x$ nanosheets in KOH or NaOH solution. In a typical reaction, 0.2 g of $Ti_3C_2T_x$ nanosheets was added into 40 mL of 2M KOH solution, stirring at room temperature for 9 h. To investigate the influence of the concentration of alkaline solutions and the reaction time, $Ti_3C_2T_x$ nanosheets were also etched in 2M KOH solution for 3h, 6h and in 0.1M or 1M KOH solution for 9 h, respectively.

Etching $Ti_3C_2T_x$ in weak alkaline solution: porous $Ti_3C_2T_x$ nanosheets can be controllably synthesized by using weak alkali such as $NH_3 \cdot H_2O$. In a typical synthesis, 0.2 g of $Ti_3C_2T_x$ nanosheets were added into 40 mL of 25-28% $NH_3 \cdot H_2O$ solution, stirring at room temperature for 9 h.

Etching $Ti_3C_2T_x$ in H_2O_2 solution: if using H_2O_2 as the reaction solution, TiO_2 nanoparticles are obtained. In a typical synthesis, 0.2 g $Ti_3C_2T_x$ nanosheets were dispersed in 40 mL of deionized water and then 20 uL of 35% H_2O_2 solution was added into this suspension, stirring at room temperature for 9 h.

The influence of O_2 on the formation of $Ti_3C_2T_x$ nanowires: 0.2 g of $Ti_3C_2T_x$ nanosheets was added into 40 mL of 2M KOH solution. Subsequently, this solution was put into a glove box, vacuumed, filled with Ar and sealed. The solution was stirred at room temperature for 9 h.

The influence of the thickness of $Ti_3C_2T_x$ nanosheets on the formation of $Ti_3C_2T_x$ nanowires: 0.2 g of multilayered $Ti_3C_2T_x$ nanosheets were added into 40 mL of 2M KOH with stirring at room temperature for 72 h.

The precipitates of above mentioned $Ti_3C_2T_x$ nanowires, porous $Ti_3C_2T_x$ nanosheets and TiO_2 nanoparticles were washed with deionized water until pH of the supernatant

reached 7.0 and collected by centrifugation. The obtained powder specimens were freeze-dried overnight.

2.2 Sample Characterization and Electrocatalytic Measurements

Sample characterization was performed by using X-ray powder diffraction (XRD), X-ray photoelectron spectra (XPS), Raman scattering spectroscopy, inductively coupled plasma (ICP) atomic emission spectroscopy, field emission gun scanning electron microscopy (FESEM), transmission electron microscopy (TEM), high resolution TEM (HRTEM), energy dispersive X-ray spectroscopy (EDX), electron energy loss spectroscopy (EELS), atomic force microscopy (AFM), and gas chromatography, etc. All electrocatalytic measurements were performed on CHI 760E electrochemical workstation (Chenhua, China) in a three-electrode cell at room temperature. The details of the equipment and experimental conditions were given in the Supporting Information.

2.3 Computational Method

The Ti-C bond length in the structural models of $Ti_3C_2T_x$ and the free-energy diagrams of electrochemical O_2 reduction were calculated by DFT calculations. The ORR is calculated in two routes, two-electron and four-electron reaction pathway. Two-electron reaction pathway is a strategy that is frequently used to take the ORR process in alkaline electrolyte into consideration.

$$* + O_2 + H_2O + e^- \rightarrow OOH^* + OH^- \quad (1)$$

$$OOH^* + e^- \rightarrow * + HO_2^- \quad (2)$$

The widely used method to consider the ORR process in alkaline electrolyte is four-electron reaction pathway:

$$* + O_2 + H_2O + e^- \rightarrow OOH^* + OH^- \quad (3)$$

$$OOH^* + e^- \rightarrow O^* + OH^- \quad (4)$$

$$O^* + H_2O + e^- \rightarrow OH^* + OH^- \quad (5)$$

$$OH^* + e^- \rightarrow * + OH^- \quad (6)$$

The details were supplied in the Supporting Information.

3. Results and discussion

Fig. 1a shows the etching path for porous $Ti_3C_2T_x$ nanosheets and crosslinked $Ti_3C_2T_x$ nanowires. $Ti_3C_2T_x$ nanosheets with various thicknesses are formed by etching Ti_3AlC_2 in HCl/LiF solution, followed by ultrasonic treatment, separated by centrifugation. The thin $Ti_3C_2T_x$ nanosheets in the upper colloidal solution were collected to fabricate $Ti_3C_2T_x$ nanowires by etching in 2M KOH or NaOH solution. At first, many pores were generated on the nanosheets, and then continue to expand with the etching process. Finally, the crosslinked $Ti_3C_2T_x$ nanowires are generated. This etching process stays in the stage of porous $Ti_3C_2T_x$ nanosheets if selecting concentrated ammonia as the etching solution [23]. **Fig. 1b-d** show the SEM images of $Ti_3C_2T_x$ nanosheets (T=F, O or OH) etched in 2M KOH solution for 0, 3 and 9 hours respectively, which distinctly demonstrate the etching process. For the convenience of description, they are labeled as $Ti_3C_2T_x$-0h, $Ti_3C_2T_x$-3h and $Ti_3C_2T_x$-9h, respectively. It is found that pores with different diameters appear on the surface of $Ti_3C_2T_x$ nanosheets after 3h, accompanied with the formation of some nanowires. After 9h, $Ti_3C_2T_x$ nanosheets are completely transformed to the crosslinked $Ti_3C_2T_x$ nanowires. TEM images (**Fig. 1e,f**) further confirm this etching process. $Ti_3C_2T_x$ nanowires are formed at the edge of $Ti_3C_2T_x$ nanosheets after etching in KOH solution for 3h, while nanopores are also observed on the surface of $Ti_3C_2T_x$ nanosheets. After 9h, only $Ti_3C_2T_x$ nanowires can be observed. HRTEM image of $Ti_3C_2T_x$-9h (**Fig. 1g**) reveals that some nanocrystals are formed along nanowires. The lattice fringes with interplanar spacings

of 0.235 and 0.154 nm are assigned to the (004) plane of anatase TiO_2 and the (110) plane of $Ti_3C_2T_x$, respectively [24,25]. The generated TiO_2 nanocrystals on $Ti_3C_2T_x$ nanowires imply the break of Ti-C bonds and the subsequent formation of Ti-O bonds during the etching process, which would be discussed later.

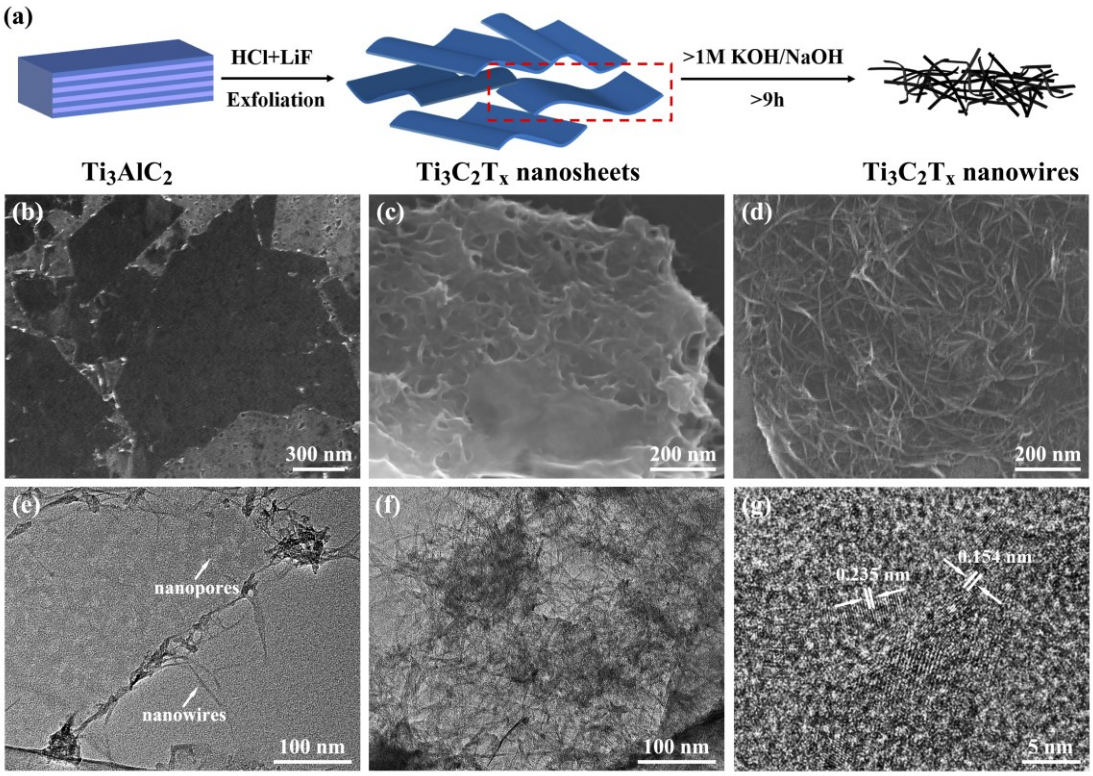

Fig. 1 (a) Illustration of the etching process for the crosslinked $Ti_3C_2T_x$ nanowires. SEM images of (b) $Ti_3C_2T_x$-0h, (c) $Ti_3C_2T_x$-3h and (d) $Ti_3C_2T_x$-9h. TEM images of (e) $Ti_3C_2T_x$-3h and (f) $Ti_3C_2T_x$-9h. (g) HRTEM image of $Ti_3C_2T_x$-9h.

It is noted that the thickness of $Ti_3C_2T_x$ nanosheets plays an important role on the structure of the final product, and thin $Ti_3C_2T_x$ nanosheets are keen to the synthesis of pure $Ti_3C_2T_x$ nanowires, e.g., a typical thickness of ~4 nm shown in **Fig. S1**. Otherwise, the composite of $Ti_3C_2T_x$ nanowires and nanosheets is obtained when thick $Ti_3C_2T_x$ nanosheets or unexfoliated multi-layered $Ti_3C_2T_x$ powder are used as the precursors

(**Fig. S2**), as reported in the literature [14-17]. Moreover, the etching time needs to extend to 72 h in order to obtain $Ti_3C_2T_x$ nanowires. The $Ti_3C_2T_x$ nanowires discussed later are all prepared by using thin $Ti_3C_2T_x$ nanosheets.

$Ti_3C_2T_x$ nanowires were further characterized by STEM-EDX. The crosslinked structure of Ti_2C_3 nanowires is distinctly observed in the HAADF image of $Ti_3C_2T_x$-9h (**Fig. S3a**). The EDX element mapping images (**Fig. S3b-f**) show the consistent distribution of Ti, O and C, derived from $Ti_3C_2T_x$ nanowires with -O- or -OH surface groups and TiO_2 nanoparticles. The amounts of -F functional groups and potassium salts are limited on $Ti_3C_2T_x$ nanowires. The typical contents of the nanowires show 50% Ti, 26% C, 24% O, while F, Cl, and K are less than 0.5%.

The crystal structure of $Ti_3C_2T_x$ was also studied by XRD. As shown in **Fig. 2a**, the XRD pattern of $Ti_3C_2T_x$-0h shows several characteristic peaks, which are assigned to the (002), (004), (006), (103), (105) and (110) planes of the $Ti_3C_2T_x$ crystal [26,27]. After etching in the KOH solution for 3 h and 9 h, the (004) and (006) peaks become indistinguishable, implying the structural transformation of $Ti_3C_2T_x$. The periodicity of $Ti_3C_2T_x$ along the c-axis is partially disrupted when $Ti_3C_2T_x$ nanosheets are converted to the porous or nanowire structure. Moreover, the (002) peak which reflects the interlayer structure of $Ti_3C_2T_x$ become very weak after etching for 9 h, also indicating the conversion of $Ti_3C_2T_x$ nanosheets to $Ti_3C_2T_x$ nanowires. The unique structure of $Ti_3C_2T_x$-0h and $Ti_3C_2T_x$-9h was then studied by the N_2 adsorption-desorption technique. The type IV isotherm with an obvious hysteresis loop (**Fig. 2b**) indicates the mesoporous structure of $Ti_3C_2T_x$-9h. Moreover, the specific surface area of $Ti_3C_2T_x$-9h is ~116.8 $m^2\ g^{-1}$, which is nine times higher than that of $Ti_3C_2T_x$-0h (~13.5 $m^2\ g^{-1}$). Although $Ti_3C_2T_x$ nanosheets have large specific surface area, they are easy to aggregate,

resulting in the decrease of surface area and loss of surface-active sites. On the contrary, the crosslinked nanowire structure can keep the large specific surface area and expose a large number of active sites. In addition, the porous structure of $Ti_3C_2T_x$-9h is conducive to the mass transport, such as the transport and adsorption of oxygen.

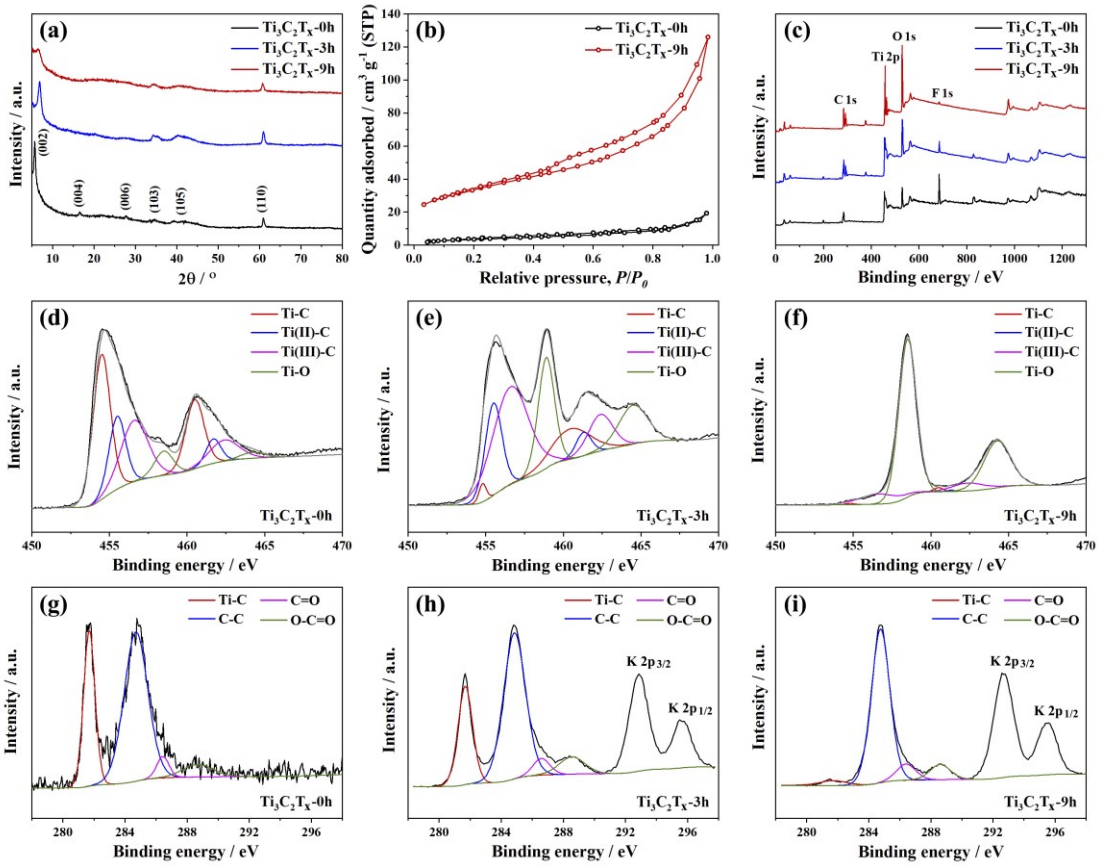

Fig. 2 (a) XRD patterns of $Ti_3C_2T_x$-0h, $Ti_3C_2T_x$-3h and $Ti_3C_2T_x$-9h. (b) N_2 adsorption-desorption isotherms of $Ti_3C_2T_x$-0h and $Ti_3C_2T_x$-9h. (c) XPS survey spectra of $Ti_3C_2T_x$-0h, $Ti_3C_2T_x$-3h and $Ti_3C_2T_x$-9h. High-resolution Ti 2p and C 1s XPS spectra of (d,g) $Ti_3C_2T_x$-0h, (e,h) $Ti_3C_2T_x$-3h and (f,i) $Ti_3C_2T_x$-9h.

XPS measurements were performed to further probe the evolution of composition and chemical bonding of $Ti_3C_2T_x$-0h, $Ti_3C_2T_x$-3h and $Ti_3C_2T_x$-9h. The XPS survey spectra of all samples (**Fig. 2c**) show four peaks of C 1s, O 1s, Ti 2p and F 1s. The C and Ti

elements originate from $Ti_3C_2T_x$, while O and F elements are related to the surface functional groups of $Ti_3C_2T_x$, such as the -O, -OH and -F terminal groups. The Al element is not observed, indicating the complete conversion of Ti_3AlC_2 to $Ti_3C_2T_x$. Furthermore, with the extension of etching time, the F 1s peak becomes very weak, while the Ti 2p and O 1s peaks become stronger, indicating that the terminal F is replaced by the terminal O by forming the Ti-OH group in alkaline media. The generated TiO_2 nanoparticles also contribute to this change. To further investigate the variation of the surface functional groups of $Ti_3C_2T_x$, the high-resolution O 1s XPS spectra of $Ti_3C_2T_x$-0h, $Ti_3C_2T_x$-0.5h, $Ti_3C_2T_x$-3h and $Ti_3C_2T_x$-9h are shown in **Fig. S4**. The O 1s peak can be divided into two separate peaks, which are assigned to Ti-O (530.0 eV) and Ti-OH (531.5 eV) bonds, respectively [28]. The ratio of Ti-OH to total O increases from 0.47 ($Ti_3C_2T_x$-0h) to 0.64 ($Ti_3C_2T_x$-0.5h), and then decreases to 0.53 ($Ti_3C_2T_x$-3h) and 0.49 ($Ti_3C_2T_x$-9h). It means that the formation of Ti-OH is very important for the etching of $Ti_3C_2T_x$. At the initial stage, the surface group of $Ti_3C_2T_x$ (e.g., F) is replaced by -OH in the alkaline solution. This process is conducive to the nucleophilic substitution reaction of OH^-, which leads to the fracture of Ti-C bonds and the formation of Ti-O bonds. Thus, the ratio of Ti-OH to total O increases first and then decreases during the etching process. Finally, TiO_2 decorated $Ti_3C_2T_x$ nanowires are prepared.

The high-resolution Ti 2p XPS spectra (**Fig. 2d-f**) show four pairs of peaks, corresponding to Ti-C (454.8, 460.5 eV), Ti(II)-C (455.5, 461.3 eV), Ti(III)-C (456.6, 462.4 eV) and Ti-O (458.5, 464.2 eV), respectively [29,30]. The obvious Ti-C, Ti(II)-C and Ti(III)-C peaks originate from $Ti_3C_2T_x$ and the Ti-O peak is related to the oxygen functional groups of $Ti_3C_2T_x$. During the etching process, the intensity of the Ti-C peak

gradually decreases and the intensity of the Ti-O peak gradually increases, also reflecting the fracture of Ti-C bonds and the formation of Ti-O bonds. It should be noted that the XPS spectra only reflect the surface composition of the sample, and cannot be used to evaluate the whole content of TiO_2 in $Ti_3C_2T_x$-9h. The C 1s peak in the high-resolution XPS spectra (**Fig. 2g-i**) can be deconvoluted into four peaks, corresponding to C-Ti (281.7 eV), C-C (284.7 eV), C-O (286.4 eV), and O-C=O (288.6 eV) bonds, respectively [31,32]. It is also found that the Ti-C peak becomes weaker during the etching process, which is consistent with the Ti 2p XPS spectra. Besides, the peaks for the K element emerge in XPS spectra of $Ti_3C_2T_x$-3h and $Ti_3C_2T_x$-9h, which may be attributed to the adsorption of potassium salt on the surface of Ti_3C_2. The C-C peak may originate from the impurities adsorbed on the sample. It is also reported that some Ti atoms could dissolve during the process of etching Al from Ti_3AlC_2, resulting in the formation of C-C bonds [33,34].

To further explore the formation mechanism of $Ti_3C_2T_x$ nanowires, we conducted several groups of control experiments. The amount of $Ti_3C_2T_x$ nanosheets used is 0.2 g in all experiments. First, the effect of the concentration of KOH solution on the etching of $Ti_3C_2T_x$ is studied. As shown in the SEM images (**Fig. 3a,b**), $Ti_3C_2T_x$ nanosheets are not completely converted into $Ti_3C_2T_x$ nanowires in 1M KOH solution for 9 h, and some nanosheets are still preserved. When the concentration of KOH solution decreases to 0.1M, only $Ti_3C_2T_x$ nanosheets are obtained. TEM image (**Fig. S5a**) shows that some pores are etched on the surface of $Ti_3C_2T_x$ nanosheets. This indicates that the etching reaction only occurs when the concentration of KOH solution (or pH value) reaches a certain level. The formation of nanowires requires at least 1M concentration of KOH. Second, the effect of the type of alkaline solution on the etching of $Ti_3C_2T_x$ is

investigated. 2M NaOH solution was used as the alkaline solution to etch $Ti_3C_2T_x$ nanosheets. The crosslinked $Ti_3C_2T_x$ nanowires are observed distinctly in the SEM and TEM images (**Fig. 3c,d**), demonstrating that $Ti_3C_2T_x$ nanowires can be obtained in either KOH or NaOH solution (strong base) as long as their concentrations are greater than 2M. When changing KOH solution to concentrated (25-28%) ammonia solution, only $Ti_3C_2T_x$ nanosheets with pores are obtained (**Fig. 3e, S5b**), similar to the result of 0.1M KOH solution. The pH value of concentrated ammonia solution (weak base) is ~11.7, even lower than that of 0.1M KOH solution. Apparently, the concentration of OH^- ions has an important influence on the etching of $Ti_3C_2T_x$. Oxygen is another important factor affecting the etching of $Ti_3C_2T_x$ because the formation of TiO_2 may promote the etching process. Therefore, $Ti_3C_2T_x$ nanosheets were also etched in 2M KOH solution in oxygen-free environment. SEM image (**Fig. 3f**) shows that some nanowires are formed at the edge of $Ti_3C_2T_x$ nanosheets, indicating that the etching process is significantly suppressed without O_2.

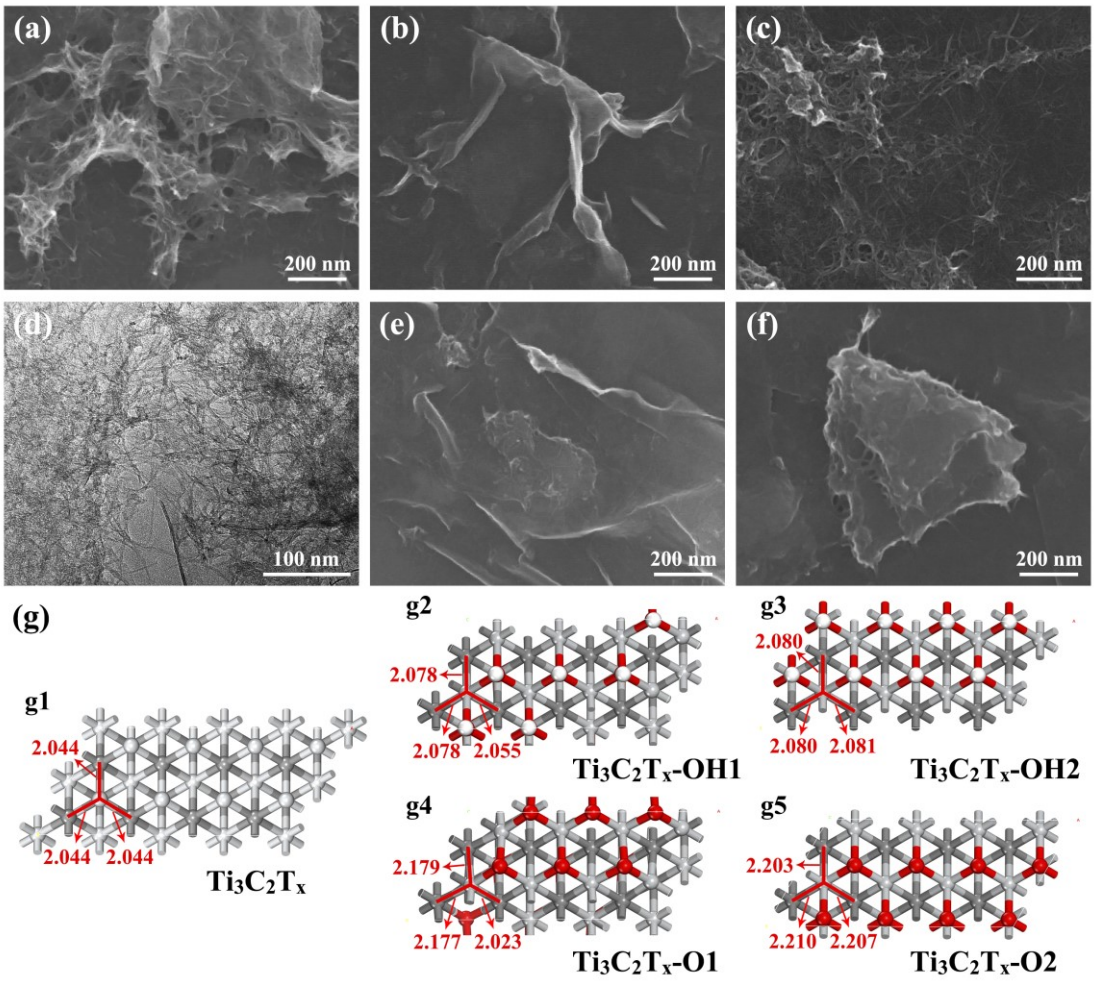

Fig. 3 SEM images of $Ti_3C_2T_x$ nanosheets etched in (a) 1M and (b) 0.1M KOH solutions for 9h. (c) SEM and (d) TEM images of $Ti_3C_2T_x$ nanosheets etched in 2M NaOH solution for 9h. SEM images of $Ti_3C_2T_x$ nanosheets etched in (e) 25-28% $NH_3 \cdot H_2O$ solution for 9h and (f) 2M KOH solution without O_2. (g) The length of the Ti-C bond in the structural model of $Ti_3C_2T_x$: (g1) without surface termination, (g2) with -OH groups at the fcc sites, (g3) with -OH groups at the hcp sites, (g4) with -O groups at the fcc sites and (g5) with -O groups at the hcp sites. Color scheme: terminal group -OH and -O (red), Titanium (light gray) and carbon (dark gray).

The above experimental results prove that OH^- and O_2 play vital roles in the etching of $Ti_3C_2T_x$. To get more insight into the etching process of $Ti_3C_2T_x$ in alkaline solution, the structure of $Ti_3C_2T_x$ and the change of Ti-C bond length are studied by DFT. First, we optimize the structure of $Ti_3C_2T_x$ after binding -OH and -O on the (001) surface of $Ti_3C_2T_x$, since the oxygen-containing groups are the main surface groups of $Ti_3C_2T_x$ in alkaline solution (see the XPS results). The four optimized structures of $Ti_3C_2T_x$-O1, $Ti_3C_2T_x$-O2, $Ti_3C_2T_x$-OH1 and $Ti_3C_2T_x$-OH2 (**Fig. S6**) are not consistent with the expected structure (**Fig. S7**) before optimization. It does not form the bridge sites for $Ti_3C_2T_x$-O1/$Ti_3C_2T_x$-OH1 and top sites for $Ti_3C_2T_x$-O2/$Ti_3C_2T_x$-OH2. On the contrary, all -O/-OH are located on hollow sites (fcc or hcp sites) [35]. It is indicated that the hollow sites are more stable than the bridge and top sites for -O/-OH occupation. Subsequently, we calculated the Ti-C bond length in five structures of $Ti_3C_2T_x$ (**Fig. 3g**). The length of the Ti-C bond is 2.044 Å for $Ti_3C_2T_x$ without surface groups. The Ti-C bond length increases to 2.078 and 2.080 Å when -OH occupies the fcc and hcp sites of $Ti_3C_2T_x$, respectively. The Ti-C bond length increases to 2.179 and 2.203 Å when -O occupies the fcc and hcp sites of $Ti_3C_2T_x$, respectively. The DFT calculations reveal that the strength of the Ti-C bond on the surface of $Ti_3C_2T_x$ is weakened after the formation of C-Ti-OH or C-Ti-O. In theory, the electron cloud of the C-Ti bond is biased toward Ti-OH according to the electronegativity of each element (C: 2.55, O: 3.44, Ti: 1.54), resulting in the decrease of the C-Ti bond strength, which is consistent with the calculated results.

Based on the above experimental results and DFT calculations, the formation mechanism of $Ti_3C_2T_x$ nanowires (**Fig. 4a**) is deduced as follows: First, the surface groups of $Ti_3C_2T_x$ (e.g., -F) are gradually replaced by -O/-OH groups in high

concentration alkaline solution (e.g., 2M KOH solution), which weakens of the C-Ti bond strength on the surface of $Ti_3C_2T_x$. This process is conducive to the nucleophilic substitution of OH^-, leading to the fracture of Ti-C bond and the falling off of $Ti(OH)_x$ species. At the same time, the exfoliated $Ti(OH)_x$ is polymerized and oxidized to TiO_2 nanoparticles, located at the edge of non-etched $Ti_3C_2T_x$. The solution after etching $Ti_3C_2T_x$ nanosheets for 9 h was analyzed by ICP. The content of titanium ions in the solution is ~8.7 mg L^{-1}, indicating that some $Ti(OH)_x$ can be formed after breaking the Ti-C bonds. Moreover, CO, CO_2, CH_4 and a trace of C_2H_4 gas were detected by gas chromatography. This indicates that the negative C exposed after breaking the Ti-C bonds would be further oxidized to CO and CO_2 or combined with H^+ to generate CH_4 and C_2H_2. Consequently, with the fracture of Ti-C bonds, some pores are initially formed on the surface of $Ti_3C_2T_x$ nanosheets. Subsequently, these pores gradually expand, resulting in the formation of the cross-linked nanowires. This process is related to the concentration of OH^- and O_2. Thus, when the concentration of OH^- and O_2 is low, the etching process can only stay at the stage of porous nanosheets. On the contrary, if the concentration of OH^- is high, nanowires are obtained. With the consumption of OH^- during the etching process, the etching process ultimately stays at the stage of nanowires. Besides, the generated TiO_2 nanoparticles will adhere to the edges of the nanowires, also preventing the attack of OH^- ions. In fact, when reducing the amount of initial $Ti_3C_2T_x$ nanosheets to ensure sufficient OH^- in solution, $Ti_3C_2T_x$ nanosheets are completely etched off.

We also attempted to etch $Ti_3C_2T_x$ nanosheets in 35% H_2O_2 solution. It is interesting to note that some pores appear on the surface of $Ti_3C_2T_x$ nanosheets after only 10 min (**Fig. S8a**). Subsequently, $Ti_3C_2T_x$ nanosheets are completely etched off after 30 min,

leaving only TiO_2 nanoparticles in solution (**Fig. S8b**). This is because H_2O_2 can release OOH^-, which has a stronger nucleophilic capability. Furthermore, H_2O_2 is a strong oxidizing agent and can also decompose to O_2. Therefore, compared to alkaline solution, H_2O_2 solution has a stronger etching ability and can completely etch off $Ti_3C_2T_x$ to form TiO_2 and carbonaceous gases.

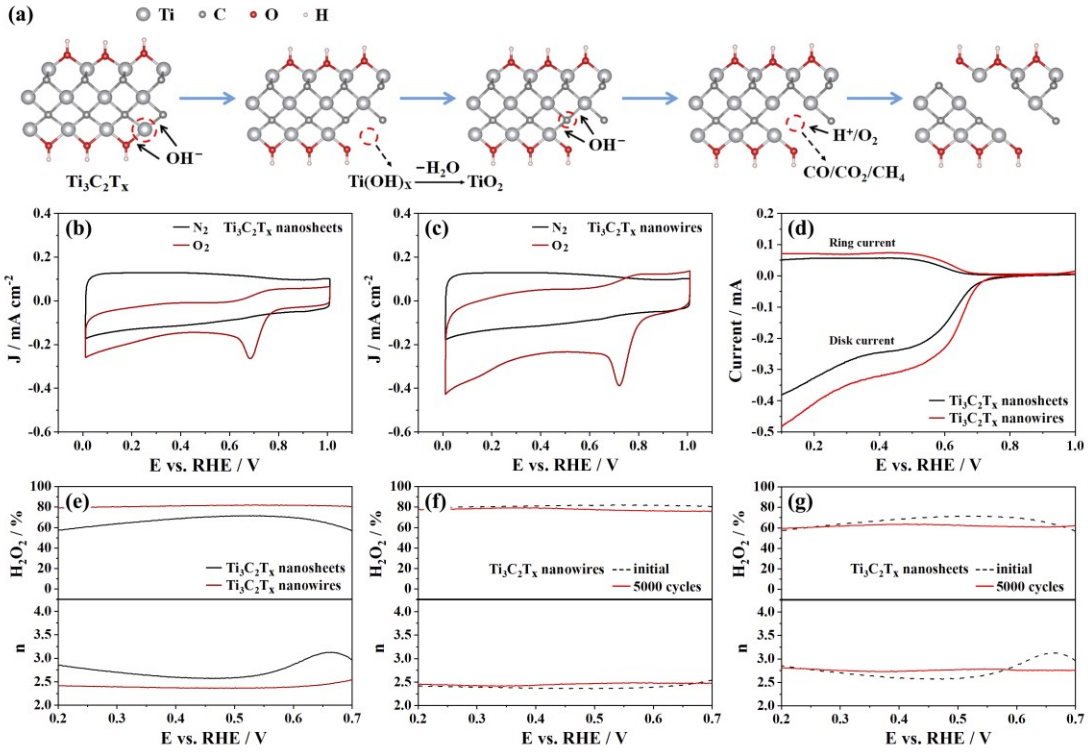

Fig. 4 (a) Mechanism diagram for the etching of $Ti_3C_2T_x$ under alkaline conditions. CV curves of (b) $Ti_3C_2T_x$ nanosheets and (c) $Ti_3C_2T_x$ nanowires in N_2 and O_2-saturated 0.1 M KOH solutions. (d) LSV curves of $Ti_3C_2T_x$ nanosheets and $Ti_3C_2T_x$ nanowires with the corresponding H_2O_2 currents recorded on the ring electrode at 1600 rpm. (e) The electron transfer number and H_2O_2 yield of $Ti_3C_2T_x$ nanosheets and $Ti_3C_2T_x$ nanowires. The electron transfer number and H_2O_2 yield of (f) $Ti_3C_2T_x$ nanowires and (g) $Ti_3C_2T_x$ nanosheets after 5000 cycles.

The performance of $Ti_3C_2T_x$ as a potential ORR catalyst was studied. A three-electrode system was used to investigate the ORR performance of $Ti_3C_2T_x$ nanosheets and $Ti_3C_2T_x$ nanowires. First, cyclic voltammetry tests were performed to evaluate the ORR activity of samples. CV curves (**Fig. 4b,c**) show no redox peaks in N_2-saturated electrolyte, but obvious oxygen reduction peaks in O_2-saturated electrolyte. This indicates that $Ti_3C_2T_x$ nanosheets and $Ti_3C_2T_x$ nanowires have ORR activity. Furthermore, the potential of the reduction peak of $Ti_3C_2T_x$ nanowires is ~0.73 V, which is more positive than that of $Ti_3C_2T_x$ nanosheets (~0.68 V), implying the higher ORR activity of $Ti_3C_2T_x$ nanowires. The polarization curves of both samples on the rotating ring-disk electrode are shown in **Fig. 4d**. The O_2 reduction current measured at the disc electrode is represented by the solid line, while the H_2O_2 oxidation current recorded at the Pt ring electrode is represented by the dash line. The onset potential and disk current of $Ti_3C_2T_x$ nanowires are 0.80 V and 0.50 mV respectively, higher than those of $Ti_3C_2T_x$ nanosheets (0.75 V and 0.40 mV), also proving that $Ti_3C_2T_x$ nanowires have better ORR activity than $Ti_3C_2T_x$ nanosheets. $Ti_3C_2T_x$ nanowires also exhibit higher ring current than $Ti_3C_2T_x$ nanosheets. It means that $Ti_3C_2T_x$ nanowires are not only a better ORR catalyst, but also a potential catalyst for H_2O_2 generation. The electron transfer numbers (*n*) and H_2O_2 yields of samples are calculated and shown in **Fig. 4e**. The *n* values of $Ti_3C_2T_x$ nanowires and $Ti_3C_2T_x$ nanosheets are 2.37 and 2.61 at 0.4 V (vs. RHE) respectively, illustrating that the ORR reaction on $Ti_3C_2T_x$ nanowires tends to occur through a two-electron transfer pathway ($O_2 + H_2O + 2e^- \rightarrow HO_2^- + OH^-$). The H_2O_2 yields of $Ti_3C_2T_x$ nanowires is 81.7% in the potential range of 0.4~0.5 V, much higher than that of $Ti_3C_2T_x$ nanosheets (70.5%), suggesting that $Ti_3C_2T_x$ nanowires could serve as a good catalyst for producing H_2O_2. The electrocatalytic stability of

$Ti_3C_2T_x$ nanowires and $Ti_3C_2T_x$ nanosheets was also studied. After 5000 cycles, the *n* value of $Ti_3C_2T_x$ nanowires is 2.45 and the H_2O_2 selectivity is kept at 78.9%, which is decreased by 2.8% (**Fig. 4f**). In contrast, the *n* value of $Ti_3C_2T_x$ nanosheets is 2.73 and the H_2O_2 selectivity (63.1%) is decreased by 7.4% (**Fig. 4g**), which is higher than $Ti_3C_2T_x$ nanowires. As a result, $Ti_3C_2T_x$ nanowires also demonstrate superior durability for ORR.

The superior ORR performance of $Ti_3C_2T_x$ nanowires is attributed to their high specific area, cross-linked structure and abundant edge active sites, which not only facilitate the transport and adsorption of O_2, but also accelerate the kinetics of ORR. Moreover, it is interesting to note that $Ti_3C_2T_x$ nanowires exhibit high activity in selectively reducing oxygen to H_2O_2.

DFT calculation was used to study the catalytic selectivity of $Ti_3C_2T_x$ nanowires. The effects of Ti and O atoms in various environments on ORR performances were examined. We created four models including surface Ti, surface O, edge Ti, and edge O (**Fig. S9**). The $2e^-$ ORR occurs following the two proton−electron transfer reactions. The O_2 molecule is converted to OOH* in the first proton–electron transfer process (see equation 1 in the Supporting Information), where * designates the catalyst's active site. HO_2^- is generated in the second proton-electron transfer reaction (see equation 2 in the Supporting Information) and is desorbed from the catalyst surface. OOH* is a critical reaction intermediate for the entire reaction, and the ORR is greatly influenced by the binding affinity of OOH*. According to the Sabatier principle, too strong or too weak binding of OOH* can adversely affect the $2e^-$ ORR. The calculated energy diagrams at 0 V following $2e^-$ ORR pathways are presented in **Fig. 5a**. The energy decreases from OOH* to H_2O_2* are very moderate for edge O, surface Ti, and surface O, but

significantly larger from O_2 to OOH*. Thus, the rate-determining step becomes the reduction of OOH* to H_2O_2* with an energy drop of 0.5, 0.18 and 0.28 eV, respectively.

Additionally, the adsorption free energy for OOH* (G_{OOH*}), which is an effective descriptor to evaluate the catalytic activity trend of the $2e^-$ ORR, is 4.2 eV, according to previous works combining measurements and DFT calculations [36,37]. ΔG_{OOH*} of edge O (~4.02 eV) is closest to 4.2 eV, indicating that edge O is the optimal reactive sites, which originates from the oxygen-containing functional groups generated during the alkali etching process and the formation of nanowire structures exposing more edge sites, in agreement with the experimental results. In **Fig. 5b**, the $4e^-$ mechanisms using Ti or O as the adsorption site were also presumptively assumed. Edge O, surface Ti, and surface O show a moderate free-energy change from OOH* to O* (**Fig. S10**). The relatively weaker adsorption strength for O* benefits the continuation of the reaction. Thus, the reduction of OH* to OH^- with an energy drop of 0.49, 0.35, and 0.35 eV, respectively, becomes the rate-determining step. The overpotential of the two-electron reaction of edge O is lower than that of the four-electron reaction. Therefore, edge O is more favorable for $2e^-$ reactions, which explains the occurrence of $2e^-$ ORR in $Ti_3C_2T_x$ nanowires.

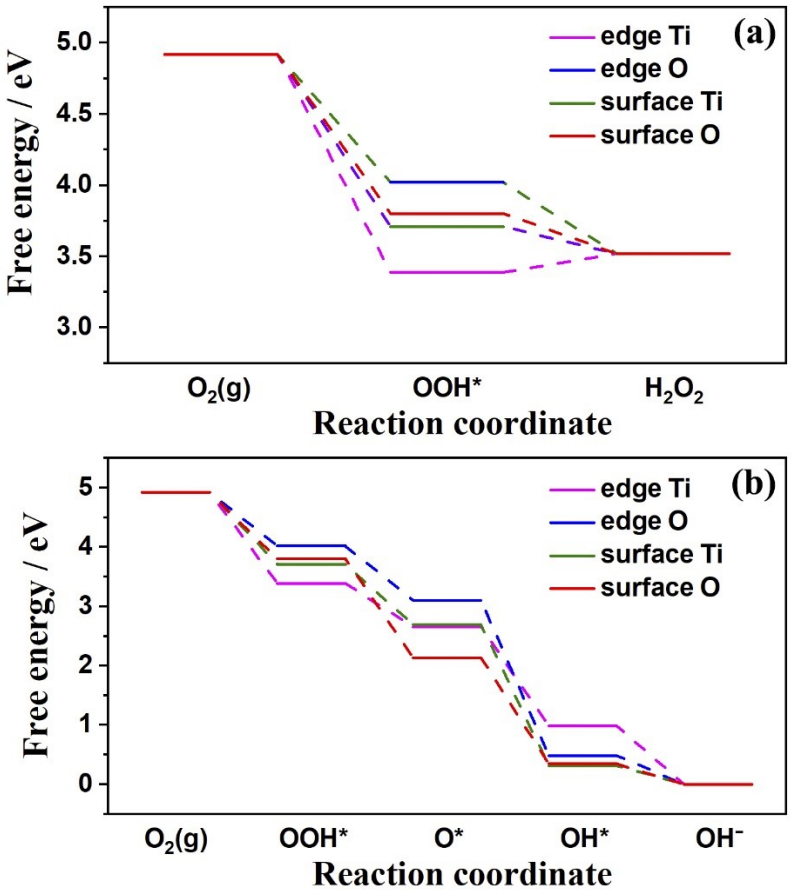

Fig. 5 (a) Free energy diagrams of $2e^-$ ORR on edge Ti, edge O, surface Ti and surface O at U = 0 V vs RHE. (b) Free energy diagrams of $4e^-$ ORR on edge Ti, edge O, surface Ti and surface O at U = 0 V vs RHE.

4. Conclusions

In summary, we have achieved controllable etching of $Ti_3C_2T_x$ nanosheets by tunning the etching conditions of alkaline solution such as alkaline type, alkaline concentration and oxygen content. The etching mechanism and the influencing factors are also studied. In the alkaline solution, the surface groups of $Ti_3C_2T_x$ nanosheets would be replaced by -O/-OH groups, which is conducive to the nucleophilic substitution of OH^-. This process leads to the fracture of Ti-C bonds and generates TiO_2 nanoparticles and gases

such as CH_4. Therefore, by controlling the concentration of alkaline solution and oxygen content, it is possible to controllably synthesize porous $Ti_3C_2T_x$ nanosheets and cross-linked $Ti_3C_2T_x$ nanowires, even $Ti_3C_2T_x$ quantum dots or TiO_2 nanoparticles. It is found that $Ti_3C_2T_x$ nanowires exhibit higher ORR activity than $Ti_3C_2T_x$ nanosheets. Moreover, the ORR reaction on $Ti_3C_2T_x$ nanowires tends to occur through a two-electron transfer pathway, suggesting the potential application of $Ti_3C_2T_x$ nanowires as a catalyst for producing H_2O_2. This study indicates that controllable regulation of $Ti_3C_2T_x$ structure can effectively expand the application fields of $Ti_3C_2T_x$ MXene.

Supporting Information

Supplementary data to this article can be found online.

Acknowledgements

This work was financially supported by National Natural Science Foundation of China (21975030).

References

[1] M. Naguib, M. Kurtoglu, V. Presser, J. Lu, J.J. Niu, M. Heon, L. Hultman, Y. Gogotsi, M.W. Barsoum, Two-dimensional nanocrystals produced by exfoliation of Ti_3AlC_2. Adv. Mater. 23 (2011) 4248–4253.

[2] H.H. Shi, P.P. Zhang, Z.C. Liu, S. Park, M.R. Lohe, Y.P. Wu, A.S. Nia, S. Yang, X.L. Feng, Ambient-stable two-dimensional titanium carbide (MXene) enabled by iodine etching. Angew. Chem. Int. Ed. 60 (2021) 8689−8693.

[3] S. Yang, P.P. Zhang, F.X. Wang, A.G. Ricciardulli, M.R. Lohe, P.W.M. Blom, X.L. Feng, Fluoride-free synthesis of two-dimensional titanium carbide (MXene) using a binary aqueous system. Angew. Chem. Int. Ed. 130 (2018) 15717−15721.

[4] M.Q. Wang, B.Y. Qin, F. Xu, W. Yang, Z.T. Liu, Y.F. Zhang, Hetero-structural and hetero-interfacial engineering of MXene@Bi_2S_3/Mo_7S_8 hybrid for advanced sodium/potassium-ion batteries, J. Colloid Interf. Sci. 650 (2023) 446-455.

[5] S.K. Li, H.R. Chai, L. Zhang, Y.C. Xu, Y. Jiao, J.R. Chen, Constructing oxygen vacancy-rich MXene @Ce-MOF composites for enhanced energy storage and conversion, J. Colloid Interf. Sci. 642 (2023) 235-245.

[6] M. Alhabeb, K. Maleski, B. Anasori, P. Lelyukh, L. Clark, S. Sin, Y. Gogotsi, Guidelines for synthesis and processing of two-dimensional titanium carbide ($Ti_3C_2T_x$ MXene). Chem. Mater. 29 (2017) 7633−7644.

[7] J. Zhang, X.Y. Zhang, W.B. Yue, Boosting electrocatalytic oxygen reduction performance of Co–N–C catalysts on Ti_3C_2 MXene by the synergistic effect with oxygen vacancy-rich TiO_2. Chem. Eng. J. 456 (2023) 141101.

[8] X. Huang, J. Song, J.J. Zhang, W. Liu, C. Zhang, W. Zhang, D.L. Wang, Investigation of MXene as oxygen reduction electrocatalyst for selective H_2O_2 generation. Nano. Res. 15 (2022) 3927-3932.

[9] L. Yan, D. Song, J.Y. Liang, X.Y. Li, H. Li, Q.B. Liu, Fabrication of highly efficient Rh-doped cobalt–nickel-layered double hydroxide/MXene-based electrocatalyst with rich oxygen vacancies for hydrogen evolution. J. Colloid Interf. Sci. 640 (2023) 338-347.

[10] Y. Wang, S. Rahimnejad, W.J. Sun, L.X. Li, H.Y. Zhang, Q. Cao, J.H. He, Bimetallic Cu-Fe catalysts on MXene for synergistically electrocatalytic conversion of nitrate to ammonia. J. Colloid Interf. Sci. 648 (2023) 595-603.

[11] H.K. Tan, L. Sun, F. Xie, J.J. Hu, Y. Qu, Y.H. Zhang, SnS nanosheets firmly bound in alkali-treated wrinkled MXene framework with enhanced lithium-ion storage. J. Colloid Interf. Sci. 633 (2023) 737-745.

[12] L.Y. Xiu, Z.Y. Wang, M.Z. Yu, X.H. Wu, J.S. Qiu, Aggregation-resistant 3D MXene-based architecture as efficient bifunctional electrocatalyst for overall water splitting. ACS Nano 12 (2018) 8017–8028

[13] X. Chia, M. Pumera, Characteristics and performance of two-dimensional materials for electrocatalysis. Nat. Catal. 1 (2018) 909-921.

[14] H.D. Shi, Y.F. Dong, S.H. Zheng, C. Dong, Z.S. Wu, Three dimensional Ti_3C_2 MXene nanoribbon frameworks with uniform potassiophilic sites for the dendrite-free potassium metal anodes. Nanoscale Adv. 2 (2020) 4212–4219.

[15] S.L. Zhang, H.J. Ying, P.F. Huang, T.T. Yang, W.Q. Han, Hierarchical utilization of raw $Ti_3C_2T_x$ MXene for fast preparation of various $Ti_3C_2T_x$ MXene derivatives. Nano Res. 15 (2022) 2746–2755.

[16] Y.F. Dong, Z.S. Wu, S.H. Zheng, X.H. Wang, J.Q. Qin, S. Wang, X.Y. Shi, X.H. Bao, Ti_3C_2 MXene-derived sodium/potassium titanate nanoribbons for high-performance sodium/potassium ion batteries with enhanced capacities. ACS Nano 11 (2017) 4792−4800.

[17] J.M. Huang, R.J. Meng, L.H. Zu, Z.J. Wang, N. Feng, Z.Y. Yang, Y. Yu, J.H. Yang, Sandwich-like $Na_{0.23}TiO_2$ Nanobelt/Ti_3C_2 MXene composites from a scalable in

situ transformation reaction for long-life high-rate lithium/sodium-ion batteries. Nano Energy 46 (2018) 20–28.

[18] P.C. Lian, Y.F. Dong, Z.S. Wu, S.H. Zheng, X.H. Wang, S. Wang, C.L. Sun, J.Q. Qin, X.Y. Shi, X.H. Bao, Alkalized Ti_3C_2 MXene nanoribbons with expanded interlayer spacing for high-capacity sodium and potassium ion batteries. Nano Energy 40 (2017) 1–8.

[19] Y.F. Dong, S.H. Zheng, J.Q. Qin, X.J. Zhao, H.D. Shi, X.H. Wang, J. Chen, Z.S. Wu, All-MXene-based integrated electrode constructed by Ti_3C_2 nanoribbon framework host and nanosheet interlayer for high-energy-density Li−S batteries. ACS Nano 12 (2018) 2381–2388.

[20] W.Y. Yuan, L.F. Cheng, Y.R. An, H. Wu, N. Yao, X.L. Fan, X.H. Guo, MXene nanofibers as highly active catalysts for hydrogen evolution reaction. ACS Sustainable Chem. Eng. 6 (2018) 8976−8982.

[21] O. Mashtalir, M. Naguib, V.N. Mochalin, Y. Dall'Agnese, M. Heon, M.W. Barsoum, Y. Gogotsi, Intercalation and delamination of layered carbides and carbonitrides. Nat. Commun. 4 (2013) 1716.

[22] M. Naguib, Y. Gogotsi, Synthesis of two-dimensional materials by selective extraction. Acc. Chem. Res. 48 (2015) 128−135.

[23] J. Zhang, X.Y. Zhang, W.B. Yue, Nanoporous nitrogen-doped Ti_3C_2 nanosheets as efficient electrocatalysts for oxygen reduction. ACS Appl. Nano Mater. 5 (2022) 11241−11248.

[24] J. Ding, Z.N. Huang, J.H. Zhu, S.Z. Kou, X.B. Zhang, H.S. Yang, Low-temperature synthesis of high-ordered anatase TiO_2 nanotube array films coated with exposed {001} nanofacets. Sci. Rep. 5 (2015) 17773.

[25] I. Persson, J. Halim, T.W. Hansen, J.B. Wagner, V. Darakchieva, J. Palisaitis, J. Rosen, P. O. A. Persson, How much oxygen can a MXene surface take before it breaks? Adv. Funct. Mater. 30 (2020) 1909005.

[26] J.Z. Zhang, N. Kong, S. Uzun, A. Levitt, S. Seyedin, P.A. Lynch, S. Qin, M.K. Han, W.R. Yang, J.Q. Liu, X.G. Wang, Y. Gogotsi, J.M. Razal, Scalable manufacturing of free-standing, strong $Ti_3C_2T_x$ MXene films with outstanding conductivity. Adv. Mater. 32 (2020) 2001093.

[27] K. Allen-Perry, W. Straka, D. Keith, S. Han, L. Reynolds, B. Gautam, D.E. Autrey, tuning the magnetic properties of two dimensional MXenes by chemical etching. Materials 14 (2021) 694.

[28] P. Zhang, R.A. Soomro, Z.R.X. Guan, N. Sun, B. Xu, 3D Carbon-coated MXene architectures with high and ultrafast lithium/sodium-ion storage. Energy Stor. Mater. 29 (2020) 163–171.

[29] V. Natu, M. Benchakar, C. Canaff, A. Habrioux, S. Célérier, M.W.A. Barsoum, A critical analysis of the X-ray photoelectron spectra of $Ti_3C_2T_z$ MXenes. Matter 4 (2021) 1224−1251.

[30] S. Myhra, J.A.A. Crossley, M.W. Barsoum, Crystal-chemistry of the Ti_3AlC_2 and Ti_4AlN_3 layered carbide/nitride phases-characterization by XPS. J. Phys. Chem. Solids 62 (2001) 811−817.

[31] M.X. Liang, L. Wang, V. Presser, X.H. Dai, F. Yu, J. Ma, Combining battery-type and pseudocapacitive charge storage in $Ag/Ti_3C_2T_x$ MXene electrode for capturing chloride ions with high capacitance and fast ion transport. Adv. Sci. 7 (2020) 2000621.

[32] R.B. Rakhi, B. Ahmed, M.N. Hedhili, D.H. Anjum, H.N. Alshareef, Effect of postetch annealing gas composition on the structural and electrochemical properties of

Ti_2CT_x MXene electrodes for supercapacitor applications. Chem. Mater. 27 (2015) 5314−5323.

[33] J. Halim, K.M. Cook, M. Naguib, P. Eklund, Y. Gogotsi, J. Rosen, M.W. Barsoum, X-ray photoelectron spectroscopy of select multi-layered transition metal carbides (MXenes). Appl. Surf. Sci. 362 (2016) 406−417.

[34] J. Halim, K.M. Cook, P. Eklund, J. Rosen, M.W. Barsoum, XPS of cold pressed multilayered and freestanding delaminated 2D thin films of $Mo_2TiC_2T_z$ and $Mo_2Ti_2C_3T_z$ (MXenes). Appl. Surf. Sci. 494 (2019) 1138−1147.

[35] M. Magnuson, L. Näslund, Local chemical bonding and structural properties in Ti_3AlC_2 MAX phase and $Ti_3C_2T_x$ MXene probed by Ti 1s X-ray absorption spectroscopy. Phys. Rev. Res. 2 (2020) 033516.

[36] Z. Lu, G. Chen, S. Siahrostami, Z. Chen, K. Liu, J. Xie, L. Liao, T. Wu, D. Lin, Y. Liu, T. Jaramillo, J. Nørskov, Y. Cui, High-efficiency oxygen reduction to hydrogen peroxide catalysed by oxidized carbon materials. Nat. Catal. 1 (2018) 156−162.

[37] X. Zhao, Y. Wang, Y. Da, X. Wang, T. Wang, M. Xu, X. He, W. Zhou, Y. Li, J. Coleman, Y. Li, Selective electrochemical production of hydrogen peroxide at zigzag edges of exfoliated molybdenum telluride nanoflakes. Natl. Sci. Rev. 7 (2020) 1360−1366.